

## Electrically Driven Spin Resonance in Silicon Carbide Color Centers

P. V. Klimov,<sup>1,2</sup> A. L. Falk,<sup>1,2</sup> B. B. Buckley,<sup>2</sup> and D. D. Awschalom<sup>1,2,\*</sup>

<sup>1</sup>*Institute for Molecular Engineering, University of Chicago, Chicago, Illinois 60637, USA*

<sup>2</sup>*Center for Spintronics and Quantum Computation, University of California, Santa Barbara, California 93106, USA*

(Received 17 October 2013; published 24 February 2014)

We demonstrate that the spin of optically addressable point defects can be coherently driven with ac electric fields. Based on magnetic-dipole forbidden spin transitions, this scheme enables spatially confined spin control, the imaging of GHz-frequency electric fields, and the characterization of defect spin multiplicity. We control defect ensembles in SiC, but our methods apply to spin systems in many semiconductors, including the diamond nitrogen-vacancy center. Electrically driven spin resonance offers a viable route towards scalable quantum control of electron spins in a dense array.

DOI: 10.1103/PhysRevLett.112.087601

PACS numbers: 76.30.Mi, 42.50.Ex, 71.70.Ej

Optically addressable paramagnetic defects in semiconductors have proven to be powerful systems for solid-state quantum control. Research into the nitrogen-vacancy (NV) center in diamond has been driven by the potential for applications in quantum information and nanoscale sensing [1–7]. More recently, intrinsic defects in SiC [8] have been shown to have similar properties to the NV center in diamond, including long coherence times that persist up to room temperature [9,10], a high degree of optical polarization [10], and spin-dependent photoluminescence [9–15]. The technological maturity of SiC growth and processing combined with defect emissions near telecom wavelengths make SiC defects particularly amenable to integration with electronic, optoelectronic, electromechanical, and photonic devices.

An important challenge in defect-spin physics is to selectively manipulate individual spins at the nanometer scale. Localized spin control is particularly important since the interspin separation required for strong dipolar coupling is on the order of tens of nanometers [16,17]. Since electric fields are readily confined on similar length scales [18], electrically driven spin resonance [19–27] could be used to address this challenge. In this Letter, we show that resonant electric fields can coherently drive spin rotations in optically addressable semiconductor point defects.

We use ac electric fields to drive Rabi oscillations across a magnetic-dipole forbidden spin transition ( $\Delta m_s = \pm 2$ ) of the optically addressable electronic spin of the QL1 defect [10] in semi-insulating 6H-SiC. We then apply our electrically driven, optically detected magnetic resonance (EODMR) technique to spatially map the QL1 spin response and the transverse ac electric field generated by our fabricated electrodes. This imaging of GHz-frequency resonant electric fields complements nonresonant kHz-frequency ac electric field sensing previously demonstrated with NV centers in diamond [4]. Since the QL1 defect shares a ground-state spin Hamiltonian with many intrinsic

defects in SiC [8–10,13,15,28–31] and the NV center in diamond [4], our results apply to a broad class of optically addressable solid-state defects.

QL1 belongs to a family of intrinsic defects in 6H-SiC known as the UD-2 family [10,32]. Our EODMR measurements determine that its optically addressable spin ( $S$ ) has integer-value, and long spin relaxation times [10] suggest that this spin is associated with its orbital ground state (see the Supplemental Material [33]). Together with its similar optical and spin transition energies to the  $S = 1$  neutral divacancies in 4H-SiC [8,9], QL1 is likely to be an  $S = 1$  neutral divacancy as well. It is  $c$ -axis oriented with  $C_{3v}$  point-group symmetry and the ground-state spin Hamiltonian [10,34]:

$$H = (hD + d_{\parallel}E_z)\sigma_z^2 + g\mu_B\boldsymbol{\sigma}\cdot\mathbf{B} - d_{\perp}E_x(\sigma_x^2 - \sigma_y^2) + d_{\perp}E_y(\sigma_x\sigma_y + \sigma_y\sigma_x), \quad (1)$$

where the  $c$  axis is oriented along the  $z$  axis,  $h$  is Planck's constant,  $\mu_B$  is the Bohr magneton,  $D = 1.299$  GHz [10] is the zero-field splitting,  $g = 2$  is the  $g$  factor,  $\boldsymbol{\sigma}$  is the vector of spin-1 Pauli matrices (see the Supplemental Material [33]),  $\mathbf{B}$  is the magnetic field vector, and  $\mathbf{E}$  is the electric field vector. The longitudinal ( $c$ -axis oriented) and transverse coefficients,  $d_{\parallel}$  and  $d_{\perp}$  respectively, couple electric fields to the spin via the Stark effect, which can arise from both spin-orbit effects [4] and perturbations to spin-spin interactions between electrons localized to QL1. The Zeeman-split energy levels due to a longitudinal magnetic field ( $B_{\parallel}$ ) are illustrated in Fig. 1(a).

The electrically driven spin resonance that we demonstrate is similar to standard magnetically driven spin resonance, except that it couples different pairs of spin eigenstates. The transverse magnetic and electric components of Eq. (1), which lead to these phenomena, can be written in the  $\sigma_z$  basis as

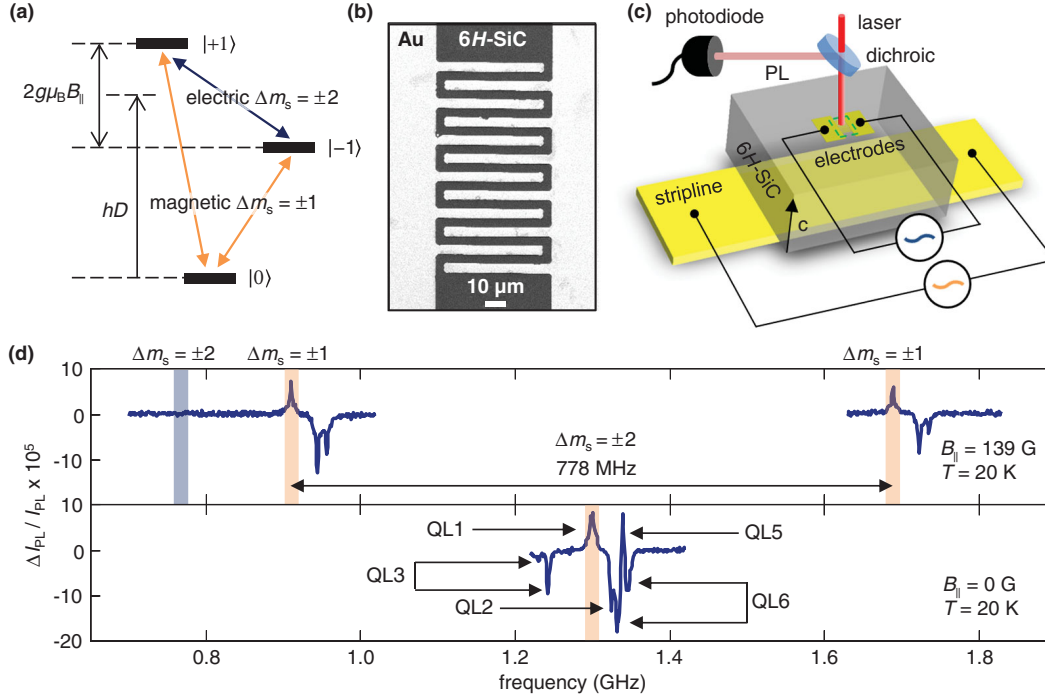


FIG. 1. (a) The orbital ground-state spin structure of the QL1 defect, with  $\Delta m_s = ±1$  transitions (orange arrows) and the  $\Delta m_s = ±2$  transition (blue arrow) indicated. (b) Scanning electron microscope image of the electrode pattern. (c) QL1 spins localized within a 400 nm thick layer immediately beneath the 6H-SiC surface are optically pumped with a 1.27 eV laser in a 1.5  $\mu\text{m}$  diameter spot, addressing  $\sim 10^4$  QL1 defects at once. Photoluminescence is filtered from the pump laser with a dichroic mirror and is measured with a photodiode. Spins are driven electrically by the electrodes and magnetically by the stripline. The electrode pattern from part (b) maps to the green dashed parallelogram. (d) The optically detected magnetic resonance (ODMR) signal when the stripline is driven at  $B_{||} = 139$  G (upper) and  $B_{||} = 0$  G (lower). The two  $\Delta m_s = ±1$  resonances are shaded orange, and the  $\Delta m_s = ±2$  resonance (at 778 MHz, shaded blue) is magnetic-dipole forbidden and not seen in ODMR.

$$H_{\perp}^B = g\mu_B(B_x\sigma_x + B_y\sigma_y) = \frac{g\mu_B}{\sqrt{2}}B_{\perp}e^{-i\phi_B}(|+1\rangle\langle 0| + |0\rangle\langle -1|) + \text{H.c.}, \quad (2)$$

$$H_{\perp}^E = -d_{\perp}E_x(\sigma_x^2 - \sigma_y^2) + d_{\perp}E_y(\sigma_x\sigma_y + \sigma_y\sigma_x) = -d_{\perp}E_{\perp}e^{i\phi_E}|+1\rangle\langle -1| + \text{H.c.}, \quad (3)$$

where  $|i\rangle$  is defined to be  $|m_s = i\rangle$ ,  $B_{\perp}$  ( $E_{\perp}$ ) and  $\phi_B$  ( $\phi_E$ ) are the magnitude and phase, respectively, of the magnetic (electric) field in the plane transverse to the  $c$  axis, and H.c. denotes the Hermitian conjugate. The main difference between  $H_{\perp}^B$  and  $H_{\perp}^E$  is that  $H_{\perp}^B$  connects triplet pairs with  $\Delta m_s = ±1$ , whereas  $H_{\perp}^E$  connects triplet pairs with  $\Delta m_s = ±2$ . As such, in the same way that applying resonant transverse magnetic fields can be used to drive magnetic-dipole ( $\Delta m_s = ±1$ ) transitions, resonant transverse electric fields can be used to drive magnetic-dipole forbidden ( $\Delta m_s = ±2$ ) transitions.

Our experiments use both ac electric and magnetic field control, for which we use separate driving elements. Open-circuit interdigitated metal electrodes on the chip's top surface are used to drive transverse electric fields between adjacent digits [Fig. 1(b)], and a short-circuited stripline beneath the chip is used to drive transverse magnetic fields

over the electrode region. A flow cryostat cools our device to the temperature  $T = 20$  K and a permanent magnet provides a static  $B_{||}$ . QL1 color centers were produced in our 6H-SiC substrates via a carbon implantation and annealing process designed to generate defects in a 400 nm thick layer immediately below the surface (see Supplemental Material [33]). The QL1 spins between adjacent electrode digits are optically addressed by non-resonantly pumping their 1.09 eV near-infrared optical transition with 1.27 eV laser light [see Fig. 1(c) and the Supplemental Material [33] for details]. In our experiments, we simultaneously address approximately  $10^4$  QL1 spins. Future efforts to extend optical addressability to the single-spin limit in SiC will use strategies such as materials purification [35], high-efficiency infrared detection, and localized ion implantation [10].

Much like the NV center in diamond [34], QL1 has a spin-dependent optical cycle, which allows nonresonant laser illumination to both polarize and read out its ground-state spin. Because its photoluminescence intensity ( $I_{PL}$ ) depends on whether its spin state is  $|0\rangle$  or  $|±1\rangle$ , we can track the QL1 spin dynamics by the measuring differential photoluminescence ( $\Delta I_{PL}$ ) between an initial state and one that has been evolved by magnetic or electric field pulses.

These  $\Delta I_{\text{PL}}$  measurements thus enable conventional (magnetically driven) optically detected magnetic resonance (ODMR) [Fig. 1(d)] and EODMR (see the Supplemental Material [33]).

We measure EODMR by implementing the sequence of spin transitions shown in Fig. 2(a) [36]. We first optically initialize the spin ensemble into  $|0\rangle$  (by convention; see the Supplemental Material [33]) and then rotate it into  $|-1\rangle$  with a magnetic  $\pi$  pulse driven on the stripline ( $\pi_B$ ). We then generate a microwave-frequency pulse ( $P$ ) on the electrodes to transfer population between  $|-1\rangle$  and  $|+1\rangle$  using electrically driven spin resonance. Any spin population remaining in  $|-1\rangle$  is transferred back into  $|0\rangle$  with another magnetic  $\pi$  pulse driven on the stripline. After this sequence, we reilluminate the sample to read out the ensemble magnetization and to reinitialize it. By modulating  $P$  on and off and measuring the locked-in  $\Delta I_{\text{PL}}$  signal, we obtain a direct measurement of  $\Delta m_s = \pm 2$  transitions driven by  $P$ .

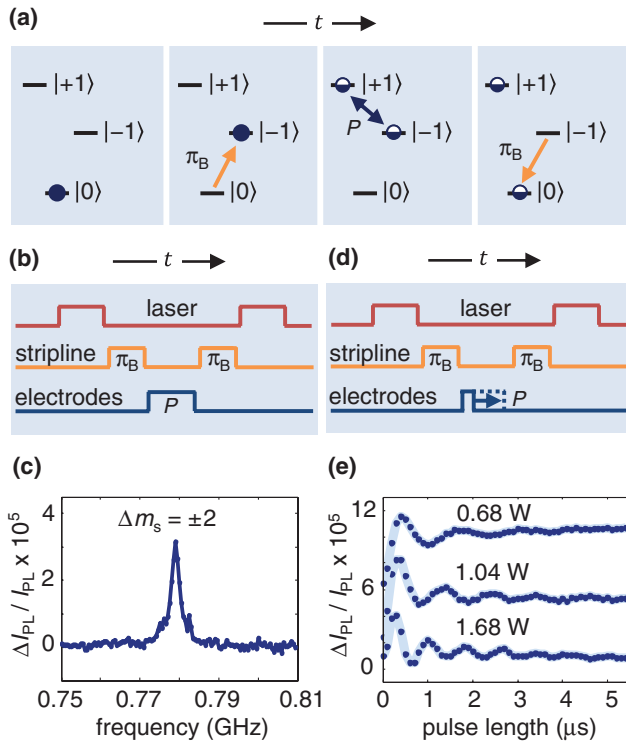


FIG. 2. (a) The sequence of spin transitions used to observe EODMR. (b) The pulse sequence used for the frequency-domain EODMR measurement. The length of  $P$  is fixed and its frequency is swept. (c) A clear EODMR feature is seen at the frequency difference of the  $|+1\rangle$  and  $|-1\rangle$  states, indicating population transfer across the  $\Delta m_s = \pm 2$  transition. The electrode power is 0.09 W and  $B_{\parallel} = 139$  G. Shoulders in the EODMR spectrum arise from hyperfine coupling to  $^{29}\text{Si}$  nuclei. (d) The pulse sequence used for the time-domain EODMR measurements. The frequency of  $P$  is fixed to the  $\Delta m_s = \pm 2$  resonance and its length is varied, resulting in (e), Rabi oscillations at three electrode driving powers. The three curves are offset for clarity.

To observe EODMR in the frequency domain, we fix the length of  $P$  and sweep its frequency [Fig. 2(b)]. This experiment returns a clear resonance at exactly the  $\Delta m_s = \pm 2$  transition frequency [Fig. 2(c)] and does not correspond to any ODMR resonances [orange shaded stripes in Fig. 1(d)]. To observe EODMR in the time domain, we fix the frequency of  $P$  to the  $\Delta m_s = \pm 2$  resonance and vary its length [Fig. 2(d)]. We observe electrically driven Rabi oscillations, whose frequency is modulated by the driving power [Fig. 2(e)]. The decay envelope is due to electric field inhomogeneity within the measurement volume and magnetic fluctuations of the coupled spin bath [37] (see the Supplemental Material [33] for data at other  $B_{\parallel}$ ).

The frequency- and time-domain data in Fig. 2 indicate driving of the  $\Delta m_s = \pm 2$  transition. However, control measurements are necessary to confirm that population transfer is driven by a transverse electric field and not by stray transverse magnetic fields from the electrodes or driving circuit. Despite the fact that the  $\Delta m_s = \pm 2$  transition is magnetic-dipole forbidden, a misalignment of the nominally longitudinal magnetic field would result in a first-order mixing of the  $|\pm 1\rangle$  and  $|0\rangle$  states and a second-order mixing of the  $|-1\rangle$  and  $|+1\rangle$  states. This mixing would then permit the nominal  $\Delta m_s = \pm 2$  transition to be weakly driven by a transverse ac magnetic field. We rule out the magnetic driving scenario by performing the following controls.

We repeat the EODMR sequence, except that now we apply  $P$  to the stripline and attempt to drive the  $\Delta m_s = \pm 2$  transition magnetically. To ensure that the transverse magnetic field is stronger in the control measurement [Fig. 3(a)] than in the EODMR measurement [Fig. 2(b)], we drive the stripline with 100 times more power than the electrodes had been driven (see the Supplemental Material [33]). As expected for magnetic driving of the  $\Delta m_s = \pm 2$  transition, a resonance is seen only when the longitudinal magnetic field is misaligned [orange curves in Fig. 3(b)]. The same misalignment has little impact on the strength of the same resonance, when driven on the electrodes, as expected for electrical driving of the  $\Delta m_s = \pm 2$  transition [blue curves in Fig. 3(b)].

We also observe that the EODMR Rabi frequency scales with the square root of the driving power, as expected [38] [Fig. 3(c)], and is independent of the  $\Delta m_s = \pm 2$  resonance frequency. The latter point further supports that the observed Rabi oscillations are driven electrically and not magnetically by displacement current through the electrodes (see the Supplemental Material [33]).

Spatially resolved EODMR allows us to investigate the extent to which spin rotations are confined by the electrodes. For these measurements, we fix  $P$  to electrically drive a  $\pi$  pulse from  $|-1\rangle$  to  $|+1\rangle$  within the electrodes, where the electric field should be strongest. We then spatially map  $\Delta I_{\text{PL}}$  while raster scanning the confocal excitation spot across the device [Figs. 4(a)–4(b)]. We observe that  $\Delta I_{\text{PL}}$  is

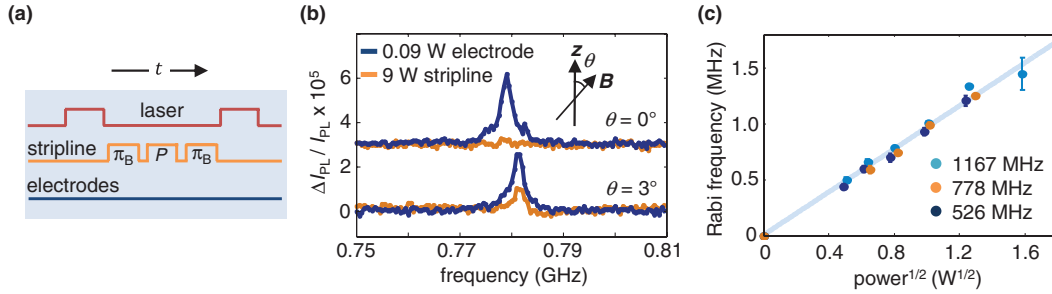


FIG. 3. (a) Pulse sequence used for the control measurement in which we attempt to drive the  $\Delta m_s = \pm 2$  transition magnetically with the stripline. The length of  $P$  is fixed and its frequency is swept. (b) A feature using the pulse sequence in (a) is only observed at the  $\Delta m_s = \pm 2$  resonance when the static longitudinal magnetic field is purposefully misaligned to the  $z$  axis (orange curves). However, EODMR (blue curves) results in a  $\Delta I_{\text{PL}}$  feature at the  $\Delta m_s = \pm 2$  resonance regardless of the magnetic field misalignment. The curves at different alignment angles are offset for clarity. (c) The electrically driven Rabi frequency scales with the square root of the driving power ( $0.92 \text{ MHz W}^{-1/2}$ ) and is independent of the  $\Delta m_s = \pm 2$  frequency (see legend). The error bars represent the 95% confidence intervals from fits to Rabi curves.

quickly extinguished away from the electrodes, and Rabi curves [Fig. 4(c)] confirm that this decrease is the result of slower spin rotations. By combining  $\Delta I_{\text{PL}}$  and  $I_{\text{PL}}$  with calibration curves (see the Supplemental Material [33]), we produce an image of the transverse ac electric field amplitude  $E_{\perp}$  [Fig. 4(d)]. This image is in good agreement with finite-element simulations of our device (see the Supplemental Material [33]) and demonstrates that

GHz-frequency electric fields can be spatially mapped with the spin of solid-state defects.

An important parameter that can be extracted from our time-domain measurements is the coupling strength between the ground-state spin and electric fields  $d_{\perp}$ . For QL1 the electric Rabi frequency scales with square root of driving power as  $0.97 \text{ MHz W}^{-1/2}$ , from which we estimate that  $d_{\perp}/h = 26 \text{ Hz cm V}^{-1}$ . When extrapolated to the  $2.4 \text{ MV cm}^{-1}$  dielectric strength of  $6H\text{-SiC}$  [39], this figure implies that 60 MHz electrically driven Rabi oscillations should be possible with QL1. In contrast to the  $g$  factor, which couples magnetic fields to the spin and is typically nearly 2 for isolated defects,  $d_{\perp}$  is highly structure dependent and material dependent [34]. Therefore, by appropriately selecting the material and defect, it might be possible to engineer the value of  $d_{\perp}$  for a broad spectrum of applications.

We introduced and implemented EODMR to demonstrate that ac electric fields can be used to coherently control the spin of optically addressable semiconductor point defects. By spatially mapping the EODMR signal around our device, we demonstrated that this technique can confine spin control between electrodes and can be used to image GHz-frequency electric fields.

In the future, applying EODMR to isolated defects in nanoscale devices could lead to the individual addressability of strongly coupled spins in a dense network. In hybrid systems, EODMR could be used for transduction between spin and other quantum mechanical degrees of freedom. Other applications could use the fact that, together, magnetic and electric fields can drive arbitrary transitions across all three spin-triplet sublevels, a promising strategy for streamlining quantum-information algorithms [40]. Electrically driven spin resonance in optically addressable defects opens many exciting prospects for scalable quantum control.

We acknowledge helpful conversations with Will Koehl, David Toyli, and Joe Heremans. This work was supported by the AFOSR, DARPA, and the NSF.

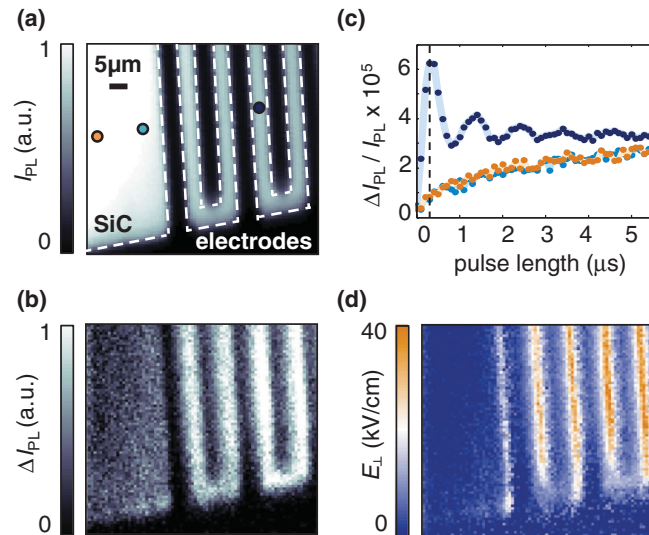


FIG. 4. (a) A map of  $I_{\text{PL}}$  in a region of the electrode device, upon continuous laser illumination. (b) Spatially resolved EODMR in the same region, with the electrode pulse ( $P$ ) power set to 1.04 W, its frequency to the 778 MHz  $\Delta m_s = \pm 2$  resonance, and its length to 300 ns. With these parameters,  $P$  induces a spin rotation from  $|-1\rangle$  to  $|+1\rangle$  between electrode digits. (c) Rabi curves taken at the three color-coded circles indicated in (a) confirm that spin rotations are confined by the electrodes. The dashed line indicates the length of  $P$ . (d) The transverse ac electric field  $E_{\perp}$  generated by the electrodes, as calculated from  $\Delta I_{\text{PL}}/I_{\text{PL}}$  (see the Supplemental Material [33]).

- \*awsch@uchicago.edu
- [1] J. R. Maze *et al.*, *Nature (London)* **455**, 644 (2008).
- [2] H. J. Mamin, M. Kim, M. H. Sherwood, C. T. Rettner, K. Ohno, D. D. Awschalom, and D. Rugar, *Science* **339**, 557 (2013).
- [3] T. Staudacher, F. Shi, S. Pezzagna, J. Meijer, J. Du, C. A. Meriles, F. Reinhard, and J. Wrachtrup, *Science* **339**, 561 (2013).
- [4] F. Dolde *et al.*, *Nat. Phys.* **7**, 459 (2011).
- [5] E. V. Oort and M. Glasbeek, *Chem. Phys. Lett.* **168**, 529 (1990).
- [6] D. M. Toyli, C. F. de Las Casas, D. J. Christle, V. V. Dobrovitski, and D. D. Awschalom, *Proc. Natl. Acad. Sci. U.S.A.* **110**, 8417 (2013).
- [7] G. Kucsko, P. C. Maurer, N. Y. Yao, M. Kubo, H. J. Noh, P. K. Lo, H. Park, and M. D. Lukin, *Nature (London)* **500**, 54 (2013).
- [8] N. T. Son *et al.*, *Phys. Rev. Lett.* **96**, 055501 (2006).
- [9] W. F. Koehl, B. B. Buckley, F. J. Heremans, G. Calusine, and D. D. Awschalom, *Nature (London)* **479**, 84 (2011).
- [10] A. L. Falk, B. B. Buckley, G. Calusine, W. F. Koehl, V. V. Dobrovitski, A. Politi, C. A. Zorman, P. X.-L. Feng, and D. D. Awschalom, *Nat. Commun.* **4**, 1819 (2013).
- [11] T. A. Kennedy, J. A. Freitas Jr., and S. G. Bishop, *J. Appl. Phys.* **68**, 6170 (1990).
- [12] N. T. Son, E. Sörman, W. M. Chen, C. Hallin, O. Kordina, B. Monemar, and E. Janzén, *Diam. Relat. Mater.* **6**, 1381 (1997).
- [13] N. T. Son, P. N. Hai, M. Wagner, W. M. Chen, A. Ellison, C. Hallin, B. Monemar, and E. Janzén, *Semicond. Sci. Technol.* **14**, 1141 (1999).
- [14] E. Sörman, N. T. Son, W. M. Chen, O. Kordina, C. Hallin, and E. Janzén, *Phys. Rev. B* **61**, 2613 (2000).
- [15] D. Riedel, F. Fuchs, H. Kraus, S. Väh, A. Sperlich, V. Dyakonov, A. A. Soltamova, P. G. Baranov, V. A. Ilyin, and G. V. Astakhov, *Phys. Rev. Lett.* **109**, 226402 (2012).
- [16] P. Neumann *et al.* *Nat. Phys.* **6**, 249 (2010).
- [17] F. Dolde, I. Jakobi, B. Naydenov, N. Zhao, S. Pezzagna, C. Trautmann, J. Meijer, P. Neumann, F. Jelezko, and J. Wrachtrup, *Nat. Phys.* **9**, 139 (2013).
- [18] N. S. Lai, W. H. Lim, C. H. Yang, F. A. Zwanenburg, W. A. Coish, F. Qassemi, A. Morello, and A. S. Dzurak, *Sci. Rep.* **1**, 110 (2011).
- [19] R. L. Bell, *Phys. Rev. Lett.* **9**, 52 (1962).
- [20] Y. Kato, R. C. Myers, D. C. Driscoll, A. C. Gossard, J. Levy, and D. D. Awschalom, *Science* **299**, 1201 (2003).
- [21] E. I. Rashba and A. L. Efros, *Phys. Rev. Lett.* **91**, 126405 (2003).
- [22] J.-M. Tang, J. Levy, and M. E. Flatté, *Phys. Rev. Lett.* **97**, 106803 (2006).
- [23] K. C. Nowack, F. H. L. Koppens, Yu. V. Nazarov, and L. M. K. Vandersypen, *Science* **318**, 1430 (2007).
- [24] E. A. Laird, C. Barthel, E. I. Rashba, C. M. Marcus, M. P. Hanson, and A. C. Gossard, *Phys. Rev. Lett.* **99**, 246601 (2007).
- [25] M. Pioro-Ladrière, T. Obata, Y. Tokura, Y.-S. Shin, T. Kubo, K. Yoshida, T. Taniyama, and S. Tarucha, *Nat. Phys.* **4**, 776 (2008).
- [26] S. Nadj-Perge, S. M. Frolov, E. P. A. M. Bakkers, and L. P. Kouwenhoven, *Nature (London)* **468**, 1084 (2010).
- [27] R. E. George, J. P. Edwards, and A. Ardavan, *Phys. Rev. Lett.* **110**, 027601 (2013).
- [28] Th. Lingner, S. Greulich-Weber, J.-M. Spaeth, U. Gerstmann, E. Rauls, Z. Hajnal, Th. Frauenheim, and H. Overhof, *Phys. Rev. B* **64**, 245212 (2001).
- [29] W. E. Carlos, N. Y. Garces, E. R. Glaser, and M. A. Fanton, *Phys. Rev. B* **74**, 235201 (2006).
- [30] J. Isoya, T. Umeda, N. Mizuochi, N. T. Son, E. Janzén, and T. Ohshima, *Phys. Status Solidi B* **245**, 1298 (2008).
- [31] A. Gali, *Phys. Status Solidi B* **248**, 1337 (2011).
- [32] B. Magnusson, and E. Janzén, *Mater. Sci. Forum* **483–485**, 341 (2005).
- [33] See Supplemental Material at <http://link.aps.org/supplemental/10.1103/PhysRevLett.112.087601> for additional data, experimental details, and theoretical considerations.
- [34] M. W. Doherty, F. Dolde, H. Fedder, F. Jelezko, J. Wrachtrup, N. B. Manson, and L. C. L. Hollenberg, *Phys. Rev. B* **85**, 205203 (2012).
- [35] S. Castelletto, B. C. Johnson, V. Ivády, N. Stavrias, T. Umeda, A. Gali, and T. Ohshima, *Nat. Mater.* **13**, 151 (2014).
- [36] E. R. MacQuarrie, T. A. Gosavi, N. R. Jungwirth, S. A. Bhave, and G. D. Fuchs, *Phys. Rev. Lett.* **111**, 227602 (2013).
- [37] V. V. Dobrovitski, A. E. Feiguin, D. D. Awschalom, and R. Hanson, *Phys. Rev. B* **77**, 245212 (2008).
- [38] R. Hanson, O. Gywat, and D. D. Awschalom, *Phys. Rev. B* **74**, 161203 (2006).
- [39] P. B. Klein, *Silicon Carbide*, edited by P. Friedrichs, T. Kimoto, L. Ley, and G. Pensl, (Wiley-VCH, Weinheim, 2010), Vol. 1, p. 288.
- [40] B. P. Lanyon, M. Barbieri, M. P. Almeida, T. Jennewein, T. C. Ralph, K. J. Resch, G. J. Pryde, J. L. O'Brien, A. Gilchrist, and A. G. White, *Nat. Phys.* **5**, 134 (2009).